

Handedness Enantioselection of Carbon Nanotubes Using Helical Assemblies of Flavin Mononucleotide

Sang-Yong Ju,^{‡,§,⊥} Darlington C. Abanulo,^{‡,⊥} Christopher A. Badalucco,[†] José A. Gascón,[†] and Fotios Papadimitrakopoulos^{*,‡,†}

[†]Nanomaterials Optoelectronics Laboratory (NOEL), Polymer Program, Institute of Materials Science and [‡]Department of Chemistry, University of Connecticut, Storrs, Connecticut 06269-3136, United States

S Supporting Information

ABSTRACT: In order to truly unlock advanced applications of single-walled carbon nanotubes (SWNTs), one needs to separate them according to both chirality and handedness. Here we show that the chiral D-ribityl phosphate chain of flavin mononucleotide (FMN) induces a right-handed helix that enriches the left-handed SWNTs for all suspended (n,m) species. Such enantioselectivity stems from the sp^3 hybridization of the N atom anchoring the sugar moiety to the flavin ring. This produces two FMN conformations (*syn* and *anti*) analogous to DNA. Electrostatic interactions between the neighboring uracil moiety and the 2'-OH group of the side chain provide greater stability to the *anti*-FMN conformation that leads to a right-handed FMN helix. The right-handed twist that the FMN helix imposes to the underlying nanotube, similar to "Indian burn", causes diameter dilation of only the left-handed SWNTs, whose improved intermolecular interactions with the overlaying FMN helix, impart enantioselection.

Molecular recognition constitutes a central scheme for enantiomeric selection in self-assembly.¹ The atomically smooth graphene surface of single-walled carbon nanotubes (SWNTs), is identified by a pair of (n,m) indices that defines their chirality.² Apart from zigzag ($n,0$) and armchair (n,n)-SWNTs, all remaining nanotube species are composed of two enantiomers, (n,m) and (m,n). By convention, when n is greater than m , the species is right-handed or *P* for positive, and when m is greater than n , the species is left-handed or *M* for negative.³ Unfortunately, current synthetic methods produce multiple (n,m)-SWNTs chiralities with both left- and right-handed species. As a result of this, numerous separation methodologies have been devised to enrich SWNTs according to chirality^{4,5} and handedness.^{3a,4b,e,6} Handedness enrichment was first introduced by the pioneering work of Komatsu et al.^{3a} via chiral diporphyrin tweezers that show a preferential adsorption toward one of the two SWNT enantiomers. Subsequent work has optimized these tweezers to fine-tune their diameter selectivity as well.⁶ In a diametrically opposed approach, Hersam's group realized that the chirality of cholates can also impart handedness-based differences in the buoyancy of nanotubes.⁷ Such buoyancy differences were exploited via density gradient ultracentrifugation (DGU),^{4e} and further resolved via the combination of co-surfactants and nonlinear

density gradients.^{4b} The interdependency of chirality and handedness separation, has prevented the field thus far to sort in one step, all left- from all right-handed SWNTs, irrespective of their (n,m) chirality.

The naturally occurring flavin mononucleotide (*R*-FMN or FMN), a phosphorylated form of vitamin B₂, was recently shown to wrap around SWNTs (Figure 1a–c) and impart

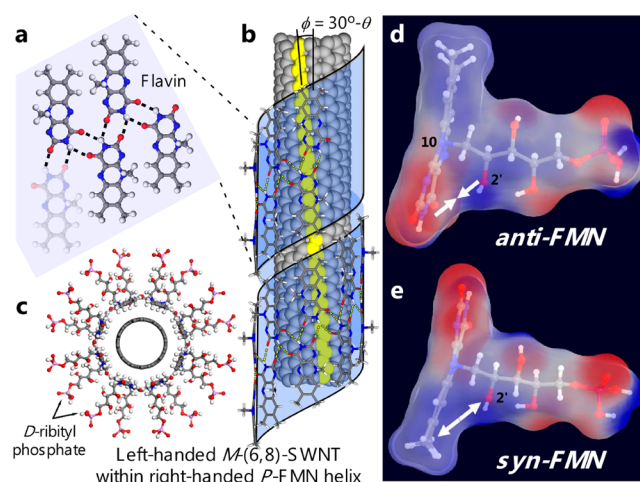


Figure 1. Adjacent H-bonds stabilize the flavin helical ribbon (a) that wraps around SWNTs (b) with the D-ribityl phosphate side groups providing aqueous solubilization (c). The sp^3 hybridization of the N(10) atom of isoalloxazine produces two conformations (d,e) for the *R*-FMN. Electrostatic attractions between the adjacent uracil and 2'-OH groups stabilize the anticonformer that leads to a right-handed FMN helix.

effective nanotube suspension with diameter distribution spanning from 0.76 to 1.17 nm, alongside (8,6)-SWNT enrichment.⁵ This is a direct result of the self-organization of isoalloxazine moieties into a 2D ribbon (Figure 1b) that subsequently wraps around SWNTs with the help of concentric π - π interactions, extending the D-ribityl phosphate side chains outward to facilitate aqueous dispersion. Ideally, four isomers are expected for each chiral-SWNT/flavin species (i.e., *P/P*, *P/M*, *M/P*, and *M/M*), with Figure 1c illustrating the *M/P* isomer. The structural similarity of FMN with nucleic acids has

Received: May 30, 2012

Published: August 7, 2012

prompted us to investigate possible handedness selection of FMN-dispersed nanotubes. Here, we show that the helical wrapping of FMN forms a right-handed helix that naturally selects all left-handed (n,m)-SWNT species.

HiPco SWNTs were dispersed in a FMN/D₂O solution using 4 h sonication (300 W) and subjected to a 2 h centrifugation (15000g) to produce an optically clear, greenish-black, nanotube dispersion, as previously reported.⁵ Figure S1a,b in the Supporting Information (SI) illustrates the well-individualized vis–NIR absorption and 2D photoluminescence excitation (PLE) spectra of D₂O FMN/SWNT dispersion, respectively.⁸ The circular dichroism (CD) and corresponding UV–vis–NIR absorption spectra of both the D₂O/FMN solution (red-curve) and the D₂O/FMN/SWNT suspension (black curve) are shown in Figure 2a,b, respectively. The

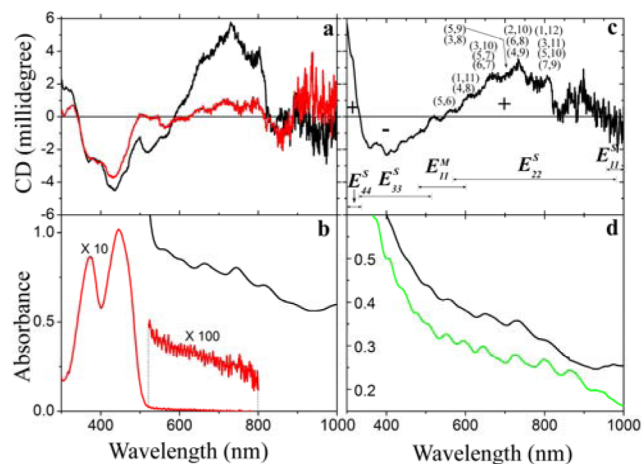


Figure 2. CD (a) and corresponding UV–vis–NIR spectra (b) of D₂O solutions of FMN (red curve) and FMN-suspended HiPco SWNTs (black curve). CD (c) and UV–vis–NIR spectra (d) following FMN replacement with SDBS (black curve). SDBS-dispersed HiPco SWNTs were used as control (green curve).

spectrum below 544 nm is overwhelmed by the FMN absorption as shown in Figure 2b. In that region, FMN exhibits a well-defined CD structure that extends at a smaller magnitude above 544 nm. The weak FMN CD spectrum above 544 nm is believed to originate from the presence of small aggregates, in accordance with the 100 times expansion of its absorption spectra in that region. On the other hand, FMN-dispersed SWNTs show a well-defined CD signal in the area of 588 and 828 nm, along with profound divergence from the FMN CD spectrum in the 300–336, 499–580, and 828–1000 nm regions.

Deciphering the true contributions of SWNTs to the CD spectra necessitates replacement of the chiral and optically absorbing FMN moiety with the achiral and optically transparent sodium dodecyl benzenesulfonate (SDBS).⁹ This was accomplished with repetitive dialysis of FMN/SWNT suspension with 1% of SDBS solution in D₂O, as previously reported.⁵ The complete SDBS replacement of the FMN moiety was confirmed by the lack of FMN PL as well as by the expected blue shift in the UV–vis–NIR absorptions of all observed (n,m) SWNTs (see Table S1, SI).⁵ On the basis of the UV–vis–NIR and PLE maps in Figure S2a,b of the SI, the aqueous SDBS-replaced SWNTs appears to be equally dispersed as the respective mother FMN/SWNT dispersion (Figure S1a,b)). Figure 2c,d illustrates the CD and UV–vis–

NIR of FMN-extracted and SDBS-replaced nanotube suspension. As expected, the elimination of FMN absorption in the 300–544 nm region, enables the observation of the underlying E_{44}^S and E_{33}^S HiPco nanotube transitions, whose regions are marked for convenience on the bottom abscissa of Figure 2c. The well-defined alternative pattern of (+,–,+) signs for the E_{44}^S , E_{33}^S , and E_{22}^S transitions, respectively, indicates that all FMN-dispersed SWNTs are left-handed enriched,⁹ and SDBS does not contribute to the CD signal (Figure S3).

The handedness enantioselectivity afforded by the FMN helix begs the question on how such separation is made possible. As shown in Figure 1d,e, a salient aspect of such handedness separation originates from the fact that the N atom at the 10 position (N(10)) of the isoalloxazine ring adopts an sp^3 hybridization that can allow the adjacent rings in the helix to closely pack with themselves.^{10,11} Such hybridization produces two different conformations for the D-ribityl chain, directing this chiral moiety in either sides of the isoalloxazine ring. These two conformations resemble the *syn* and *anti* conformations between glycoside and purine/pyrimidine bases of DNA. The *syn* and *anti* conformations are responsible for the formation of left-handed (i.e., Z-form) and right-handed (i.e., A- and B-form) DNA, respectively.¹² Figure 1d,e depicts the two energy-minimized conformations of FMN at the DFT/B3LYP/6-31g+(d,p) level of theory, with the hybridization of the N(10) atom fixed as sp^3 (see Methods in SI). This causes the D-ribityl phosphate side chain to reside in either side of the isoalloxazine ring, which in turn directs the polar uracil moiety closer to (*anti*) or farther from (*syn*) the 2'-hydroxyl group. The computed energy difference between the two conformers is 3.0 (1.5) kcal/mol in vacuum (water), in favor of the *anti* conformer. Such energy difference stems mainly from electrostatic interactions between the 2'-hydroxyl's dipole and the oppositely oriented dipoles of the uracil's C=N and C=O groups. The mapping of the DFT-derived electrostatic potential into the molecular surface shows that the *anti* conformer is electrostatically favored (i.e., complementary blue/red charge coloration denotes attractive interactions) as opposed to the repulsive interactions in the *syn* conformer. Since electrostatic interactions are inversely proportional to distance, the hydroxyl groups further up in the D-ribityl side chain contribute much less to the difference in energy. In accordance with DNA, the *anti*-like conformation of FMN prefers to organize in right-handed helices, as shown in Figure 1c. This is directly supported by HRTEM images published elsewhere,⁵ where only right-handed helices have been observed.

The next question pertains on why the right-handed helix selects left-handed nanotubes? The two leading models invoke structural rearrangement of the FMN helix alone or some sort of “cooperative interaction” between the nanotube/FMN helices. To address the first model, we investigated the orientation tendency of the isoalloxazine rings with respect to its underlying chiral lattice, within the tight confines of the 8_1 helix. For this, we used molecular mechanics (MM) force-field calculations on the two handedness isomers of (8,6)-SWNT (i.e., *P*-(8,6) and *M*-(6,8)), since our originally predicted structure of the 8_1 helix⁵ showed good agreement with that from a more advanced DFT calculation.¹¹ This allowed us to incorporate periodic boundary conditions for both FMN and nanotube helices by slightly contracting (ca. 5%) the 2.63 nm (8,6)-SWNT unit cell¹⁵ to match the 2.5 nm helix period.⁵

Figure 3a,b illustrates a close-up of the starting and the energy-minimized FMN configuration (two out of the eight Σ_n

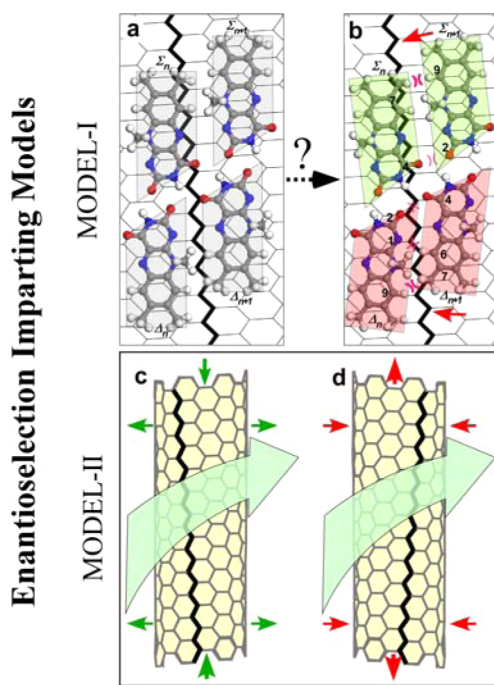


Figure 3. Two plausible models on the nature of nanotube enantioselection. Model-I: Molecular simulations on FMN rotation on rigid *M*-(6,8)- or *P*-(8,6)-SWNTs (Figure S4) indicate that the starting, “armchair-like” orientation of the isoalloxazine moieties (a) causes the Σ_n and Δ_n sub-helices to rotate opposite to each other (b). This casts doubts on the validity of this model for imparting SWNT enantioselection since the energy gains from the green-shaded Σ_n sub-helix (with optimum lattice registry) are nullified by the red-shaded Δ_n sub-helix. Model-II: The right-handed FMN helix (green arrow) exerts torsion to the nanotube similar to “Indian burn” that in the case of left-handed chiral SWNTs causes axial compression and diameter dilation (c) as opposed to right-handed nanotubes that creates axial elongation and diameter contraction (d). Here, (c) is preferred over (d) since diameter dilation enhances the intermolecular interactions between FMN helix and SWNT.

and Δ_n isoalloxazine repeats) of the right-handed FMN helix around a rigid *M*-(6,8)-SWNT (*P*-(8,6)-nanotube is shown in Figure S4). Here it is important to stress that the atomic coordinates for both *M*-(6,8) and *P*-(8,6)-SWNTs were held constant and were not allowed to relax, while the *P*-FMN helix was left free to optimize itself with respect to the underlying graphene pattern. The nanotube handedness is illustrated by the “polyacetylene chain” shown in thicker tone, while the overlaid trapezoid indicates an idealized footprint of the isoalloxazine ring. For the sake of clarity, the nanotubes in Figure 3,b are depicted in a flattened projection (i.e., hexagons stretched laterally), while Figures S5 and S6 show the longitudinal and axial projections, respectively, to illustrate the full helical pattern along with dimethyl group interdigitation developed via energy minimization. The starting *P*-FMN helix has the isoalloxazine rings oriented parallel with the longitudinal nanotube axis. Upon energy minimization, all eight Σ_n subunits rotate clockwise so that they orient along the nanotube lattice registry. Having said this, the strong H-bonding that holds the FMN ribbon together (Figure 1b) acts as a pivotal point and causes the remaining Δ_n subunits to rotate in the opposite direction. Consequently, while the Σ_n subunits improve their π - π stacking interactions (green shading) the Δ_n moieties end up with a poorer alignment.

No matter how carefully we attempted to align both Σ_n and Δ_n moieties along the polyacetylene chain, the lateral close packing of the helix along with the specific H-bonding pattern eventually forced them to rotate opposite to each other.

A direct consequence of such opposite rotation is the development of a number of close contacts shown in Figure 3b and analyzed in Table S2. The two prominent close contacts (2.4–2.6 Å) are between the two hydrogen atoms at the C₉ position for the Δ_n units, and the two hydrogens of the methyl group at the 7 position for the Σ_n units. Two other close contacts of lesser severity are that for N₁ to H–C₆ (2.6–2.7 Å) and for C₂=O to O=C₄ (2.8–2.9 Å). Here it is important to note that while the methyl group at the N₁₀ position appears to be in close proximity to the nearest isoalloxazine ring, the N₁₀ sp³ configuration permits this methyl group to lie above the aromatic ring plane and thus renders it nonrelevant in terms of close contacts. Tables S3 and S4 along with Figures S5 and S6 illustrate the breakdown in terms of energy contribution from bonds, angles, torsions, inversions, and van der Waals (vdW), electrostatic, and H-bonding interactions for both *M*-(6,8) and *P*-(8,6)-SWNTs wrapped with *P*-FMN helix. As it turns out, the right *P*-FMN helix produces a slightly more stable assembly around a *M*-(6,8)-SWNTs (by 1.2 kcal/mol or 52 meV) as compared to *P*-(8,6)-SWNTs. Taking into consideration the fact that the average H-bonding energy is comparable for Σ_n/Δ_n and Σ_n/Δ_{n+1} pairs for both complexes (Figure S7), it is safe to conclude that half of stabilization (0.6 kcal/mol) can be ascribed from improved vdW between FMN helix and nanotube, while the other half is attributed to internal (bonded and nonbonded) stabilization within the FMN helix on the *M*-(6,8)-SWNT (Table S3). This puts in question whether such small energy difference (ca. $2k_B T$) can explain enantioselection for such a large assembly, hence the question mark above the dotted arrow in Figure 3. Moreover, since the FMN rotation of Model-I is limited to small angles of ϕ (ca. 5–6° before close contacts render it prohibitive), it becomes apparent that structural rearrangement of FMN alone cannot fully address the experimental results of Figure 2, where enantioselection for nanotubes with much larger ϕ or smaller chiral angles θ ($\phi \approx 30^\circ - \theta$) occurs.

With this in mind, we redirect our focus to the second model (Model-II) where enantioselectivity originates from a “cooperative interaction” between the nanotube and its FMN helix. One possibility is that the right-handed FMN helix due to its close-packed nature, imposes a right twist to the nanotube resembling “Indian burn”. Recent reports show that small nanotube twists are not that energetically expensive, and can certainly be accommodated within $k_B T$.^{14,15} Such a twist, could (in principle) improve intermolecular interactions of both Σ_n and Δ_n moieties with the underlying graphene lattice. Using classical molecular dynamics based on second-generation reactive empirical bond order (REBO) potentials that sufficiently describe C–C interactions in graphite and diamond, Upmanyu et al.¹⁶ has shown that all (*n,m*) chiral nanotubes exhibit asymmetric torsional response to an externally applied strain. What is more important, however, is that twisting chiral nanotubes toward the armchair configuration causes them to compress axially and dilate radially (Figure 3c). On the other hand, a twist in the opposite direction (toward the zigzag configuration) causes them to expand axially and shrink diametrically (Figure 3d). This indicates that when a right-handed twist is applied to all left-handed *M*-(*m,n*) nanotubes,

Table 1. Resonance Raman RBM and ω_{G^+} Shifts of Sodium Cholate (SC) and FMN (with Low Coverage (*lc*) and High Coverage (*hc*)) Dispersed SWNTs of Varying Chiral Angle θ

(n,m)	θ (°)	E_{laser} (eV)	ω_{RBM} (cm ⁻¹)			$\Delta\omega_{\text{RBM}}$ (cm ⁻¹)		ω_{G^+} (cm ⁻¹)			$\Delta\omega_{G^+}$ (cm ⁻¹)	
			SC	FMN, <i>lc</i>	FMN, <i>hc</i>	<i>hc</i> - <i>lc</i>	SC - <i>hc</i>	SC	FMN, <i>lc</i>	FMN, <i>hc</i>	<i>hc</i> - <i>lc</i>	SC - <i>hc</i>
(7,5)	24.5	1.96	283.4	286.8	287.8	1.0	4.4	1594.5	1595.4	1593.6	-1.8	-0.9
(10,2)	8.9	1.58	265.8	266.4	267.7	1.3	1.9	1592.9	1592.8	1591.0	-1.8	-1.9

these should exhibit improved intermolecular interactions between nanotube and FMN helix due to diameter dilation.

To ascertain whether the FMN helix induces SWNT torsion, we resorted to resonance Raman spectroscopy (RRS). Knowing that increasing amount of FMN improves nanotube coverage and helix perfection,⁵ we performed RRS on SWNTs with low and high FMN coverage (*lc* and *hc*, respectively; see Methods in SI and Figures S8 and S9). It is well known that nanotube twist incurs a frequency downshift on the longitudinal G-band.¹⁷ This trend is observed with increasing coverage, as shown by the $\Delta\omega_{G^+}$ (*hc* - *lc*) column in Table 1, despite an otherwise expected upshift due to FMN-induced nanotube *p*-doping.¹¹ In terms of radial breathing mode (RBM), nanotube torsion has been reported to upshift ω_{RBM} .^{17a} This is witnessed with all resolvable (n,m) nanotubes in Table 1 (Figure S9), using the two laser lines that are above 600 nm to avoid FMN fluorescence. Here, the FMN-induced charge transfer⁵ provides an initial stiffening of the FMN/SWNT complex, causing an appreciable upshift with respect to the ω_{RBM} of sodium cholate (SC)-dispersed SWNTs. By increasing FMN coverage, an additional upshift is witnessed ($\Delta\omega_{\text{RBM}}$ (*hc* - *lc*) column). Furthermore, the increasing magnitude in $\Delta\omega_{\text{RBM}}$ shift for nanotubes with increasing chiral angle (θ) provides an additional indication in support of FMN-induced nanotube twist ($\Delta\omega_{\text{RBM}}$ (SC - *hc*) column).^{17c} These RRS findings provide strong initial support that the observed enantioselection is linked with FMN-induced nanotube twisting (Model II). Having said this, more refined molecular simulations together with tunable excitation RRS studies are needed in order to resolve more (n,m) -SWNTs and fully quantify the interplay between nanotube twist and FMN-induced torsion, to be investigated in future publications. These studies can ultimately decipher whether nanotube twisting is the cause of the unique, FMN-induced, family- and modality-dependent red-shift pattern, observed in ref 5, as well as DGU-based SWNT enantioselection,^{4b} via handedness-specific diameter variations.

■ ASSOCIATED CONTENT

📄 Supporting Information

Methods, UV-vis-NIR, PLE maps, RRS, and molecular mechanics analysis. This material is available free of charge via the Internet at <http://pubs.acs.org>.

■ AUTHOR INFORMATION

Corresponding Author

papadim@mail.ims.uconn.edu

Present Address

[§]Department of Chemistry, Yonsei University, Seoul, Korea

Author Contributions

[†]S.-Y.J. and D.C.A. contributed equally.

Notes

The authors declare no competing financial interest.

■ ACKNOWLEDGMENTS

Financial support by AFOSR FA9550-09-1-0201, and in part by NSF IIP-0930494 and CBET-0828771/0828824 and NIH ES013557, is kindly acknowledged.

■ REFERENCES

- (1) (a) Cram, D. J. *Science* **1988**, *240*, 760. (b) Maier, N. M.; Franco, P.; Lindner, W. J. *Chromatogr. A* **2001**, *906*, 3.
- (2) Wildöer, J. W. G.; Venema, L. C.; Rinzler, A. G.; Smalley, R. E.; Dekker, C. *Nature* **1998**, *391*, 59.
- (3) (a) Peng, X.; Komatsu, N.; Bhattacharya, S.; Shimawaki, T.; Aonuma, S.; Kimura, T.; Osuka, A. *Nat. Nanotechnol.* **2007**, *2*, 361. (b) Strano, M. S. *Nat. Nanotechnol.* **2007**, *2*, 340.
- (4) (a) Tu, X.; Manohar, S.; Jagota, A.; Zheng, M. *Nature* **2009**, *460*, 250. (b) Ghosh, S.; Bachilo, S. M.; Weisman, R. B. *Nat. Nanotechnol.* **2010**, *5*, 443. (c) Liu, H.; Nishide, D.; Tanaka, T.; Kataura, H. *Nat. Commun.* **2011**, *2*, 309. (d) Nish, A.; Hwang, J. Y.; Doig, J.; Nicholas, R. J. *Nat. Nanotechnol.* **2007**, *2*, 640. (e) Arnold, M. S.; Green, A. A.; Hulvat, J. F.; Stupp, S. I.; Hersam, M. C. *Nat. Nanotechnol.* **2006**, *1*, 60.
- (5) Ju, S. Y.; Doll, J.; Sharma, I.; Papadimitrakopoulos, F. *Nat. Nanotechnol.* **2008**, *3*, 356.
- (6) (a) Peng, X.; Komatsu, N.; Kimura, T.; Osuka, A. *J. Am. Chem. Soc.* **2007**, *129*, 15947. (b) Peng, X.; Komatsu, N.; Kimura, T.; Osuka, A. *ACS Nano* **2008**, *2*, 2045. (c) Wang, F.; Matsuda, K.; Rahman, A. F. M. M.; Peng, X.; Kimura, T.; Komatsu, N. *J. Am. Chem. Soc.* **2010**, *132*, 10876.
- (7) Green, A. A.; Duch, M. C.; Hersam, M. C. *Nano Res.* **2009**, *2*, 69.
- (8) Bachilo, S. M.; Strano, M. S.; Kittrell, C.; Hauge, R. H.; Smalley, R. E.; Weisman, R. B. *Science* **2002**, *298*, 2361.
- (9) Dukovic, G.; Balaz, M.; Doak, P.; Berova, N. D.; Zheng, M.; McLean, R. S.; Brus, L. E. *J. Am. Chem. Soc.* **2006**, *128*, 9004.
- (10) (a) Kierkegaard, P.; Norrestam, R.; Werner, P.-E.; Csöreg, I.; von Glehn, M.; Karlsson, R.; Leijonmark, M.; Rönquist, O.; Stensland, B.; Tillberg, O.; Torbjörnsson, L. In *Flavins and Flavoproteins, Third International Symposium*; Kamin, H., Ed.; University Park Press: Baltimore, 1971; pp 1–22. (b) Beinert, W.-D.; Ruterjans, H.; Müller, F. *Eur. J. Biochem.* **1985**, *152*, 573.
- (11) Ogunro, O. O.; Wang, X. Q. *Nano Lett.* **2009**, *9*, 1034.
- (12) (a) Blackburn, G. M.; Gait, M. J. *Nucleic Acid and Chemistry and Biochemistry*, 2nd ed.; Oxford University Press: New York, 1996; pp 24–25. (b) Dickerson, R. E.; David, M. D. *Methods in Enzymology*; Academic Press: San Diego, CA, 1992; Vol. 211, p 67.
- (13) Dresselhaus, M. S.; Dresselhaus, G.; Avouris, P., Eds. *Carbon nanotubes: Synthesis, Structure, Properties and Applications*; Springer: Berlin, 2001.
- (14) (a) Kwon, Y. K.; Tománek, D. *Phys. Rev. Lett.* **2000**, *84*, 1483. (b) Wang, S.; Wang, R.; Wu, X.; Zhang, H.; Liu, R. *Phys. E Low Dimens. Syst. Nanostruct.* **2010**, *42*, 2250.
- (15) Liu, Z.; Qin, L. C. *Carbon* **2005**, *43*, 2146.
- (16) Liang, H.; Upmanyu, M. *Phys. Rev. Lett.* **2006**, *96*, 165501.
- (17) (a) Gao, B.; Duan, X.; Zhang, J.; Wu, T.; Son, H.; Kong, J.; Liu, Z. *Nano Lett.* **2007**, *7*, 750. (b) Li, X.; Jia, Y.; Dong, J.; Kawazoe, Y. *Phys. Rev. B* **2010**, *81*, 195439. (c) Yang, L.; Han, J. *Phys. Rev. Lett.* **2000**, *85*, 154.

Handedness Enantioselection of Carbon Nanotubes using Helical Assemblies of Flavin Mononucleotide

Sang Yong Ju^{†,§}, Darlington C. Abanulo[†], Christopher A. Badalucco[‡], José A. Gascón[‡], and Fotios Papadimitrakopoulos^{†,‡,*}

Contribution from the Nanomaterials Optoelectronics Laboratory (NOEL), Polymer Program[†],
Department of Chemistry[‡], Institute of Materials Science, University of Connecticut, Storrs,
Connecticut 06269-3136

§ Present address: Department of Chemistry, Yonsei University, Seoul, Korea

* Correspondence E-mail: papadim@mail.ims.uconn.edu

Table of Contents	S1
Methods	S2
Table S1. E_{22}^S transitions of FMN-extracted and SDBS-replaced SWNTs.....	S5
Table S2. Isoalloxazine close contacts (Å) for <i>M</i> -(6,8)- and <i>P</i> -(8,6)-SWNT within <i>P</i> -FMN helices	S6
Table S3. Molecular mechanics (MM) energy contributions for <i>M</i> -(6,8) and <i>P</i> -(8,6)-SWNT within <i>P</i> -FMN helices.....	S7
Table S4. Isoalloxazine sub-helix pair (<i>i.e.</i> $\Sigma_n - \Sigma_{n+1}$ and $\Delta_n - \Delta_{n+1}$) energy contributions.....	S8
Figure S1. UV-Vis-NIR & PLE map of FMN-wrapped HiPco SWNTs	S9
Figure S2. UV-Vis-NIR & PLE map of FMN-dispersed and SDBS-replaced HiPco SWNTs	S9
Figure S3. Circular dichroism (CD) of SDBS-dispersed HiPco SWNTs	S10
Figure S4. Starting and MM minimized configuration of <i>P</i> -FMN helix around <i>M</i> -(6,8) and <i>P</i> -(8,6)-SWNTs.....	S11
Figure S5. 3-D rendering of Figure S3 along with variations in vdW and total energy contributions for each FMN and FMN-sub-helices.....	S12
Figure S6. Starting and minimized dimethyl group conformations for adjacent FMN moieties.....	S12
Figure S7. Average H-bonding energies between Σ_n and Δ_n isoalloxazine moieties	S13
Figure S8. Resonance Raman Spectra of SC- and FMN-dispersed SWNTs (with low (<i>lc</i>) and high (<i>hc</i>) FMN coverage).....	S14
Figure S9. Nanotube assignment based on PLE-derived E_{22}^S transitions against RBM-calculated resonances for SC- and FMN-dispersed SWNTs	S15
References	S16

METHODS

Materials and instrumentation: Flavin mononucleotide (FMN, 85%), sodium dodecyl benzene sulfonate (SDBS) and sodium cholate (SC) were purchased from Aldrich. Deuterated water (D₂O) was obtained from Acros and used as received. Single-walled carbon nanotubes (SWNT) prepared by high pressure carbon monoxide process (HiPco, Lot# P0339, with diameter (d_t) distribution 1.00 ± 0.35 nm) were produced by Carbon Nanotechnologies Inc. Centrifugation-assisted dialysis tubes (Centricon, MW cutoff 3,000, maximum centrifugation speed 5000 g) were obtained from Millipore. Precautions were taken to avoid prolonged exposure of FMN to direct sunlight by carrying the experiments in a laboratory equipped with yellow lights. Fluorescence spectroscopy measurements were conducted on a Jobin-Yvon Spex Fluorolog 3-211 spectrofluorometer equipped with a PMT near-infrared (NIR) detector with 3 nm step size in both excitation and emission wavelength. Both excitation and emission light intensities were corrected against instrumental variations using Spex Fluorolog sensitivity correction factors. The UV-Vis-NIR absorption spectra were measured with a Perkin-Elmer Lambda 900 UV-Vis-NIR spectrometer. Circular dichroism (CD) spectra was obtained by Pi Star (Applied Photophysics) equipped with water circulator to maintain tight temperature control at 20°C. A cuvette with path-length of 5 mm was used for all experiments. All samples were kept at the given temperature for at least 20 min prior to spectra collection to allow thermal and convectional equilibration. To improve the signal-to-noise ratio, first CD was scanned over entire region between 300 - 1000 nm. Based on this, the CD spectrum from 300 to 1000 nm were collected from sector 300 - 500, 500 - 800, 800 - 1000 nm with progressively larger number of scan, respectively.

Dispersion & titration method:

FMN-HiPco and SC-HiPco suspension protocol: A mixture of 1 mg of HiPco SWNT¹ and 4 mg of FMN were added into 4 mL of D₂O, according to previously published report.² The solution was sonicated for 4 hrs at 300W intensity. The resulting greenish-dark solution was centrifuged at 15 kg for 2 hr and the supernatant (upper 90 %) was carefully collected, to remove any bundled carbon nanotubes, to produce a clear greenish-dark solution. Similarly, 1 mg of HiPco SWNT¹ were sonicated in 10 ml of a 2 wt% aqueous of SC. For further individualization, the resulting suspension underwent centrifugation at 300 kg for 4 hours to obtain a grey nanotube suspension.

Replacement of FMN with SDBS in FMN-HiPco sample: Initially, 2 mL of FMN-HiPco sample was dialyzed using a Centricon (Millipore, 3000 molecular weight cut off filter) *via* centrifugation at 5,000 g for 1 hr. 2 ml of 1 wt. % of sodium dodecyl benzene sulfate (SDBS) in D₂O was added to this filtrate, shaken mildly and re-dialyzed using 1 hr. centrifugation through the same Centricon. This process was repeated for at least 7-8 times until the resulting filtrate was devoid of the distinct green fluorescence emission of FMN. The resulting precipitate was re-suspended in 4 ml of 1 wt. % of SDBS in D₂O in

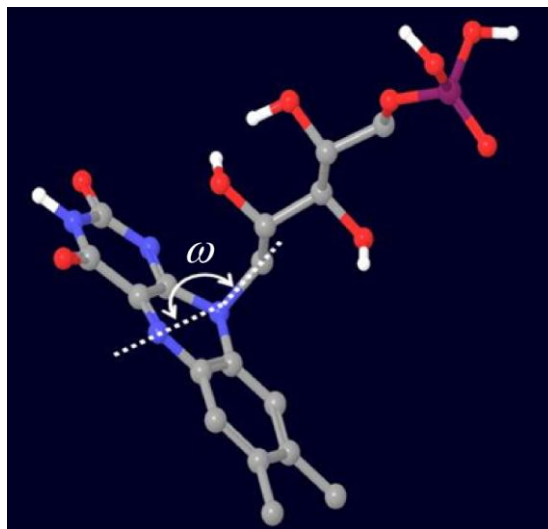
order to accommodate the limited solubility of SWNT in aqueous SDBS and was bath-sonicated for 6 hr at 20 °C to individualize the majority of nanotubes.

Resonance Raman Spectroscopy: Under the same experimental conditions (laser intensity, focus, exposure time and collection scan number for a given laser line), resonance Raman spectra were collected with a Renishaw Ramanscope in the backscattering configuration, with E_{laser} excitations of 633 nm (1.95 eV) and 785 nm (1.58 eV) lasers from all three samples: (i) SC- dispersed SWNTs prepared in the aforementioned protocol, (ii) and (iii) FMN dispersed SWNTs with 1mg/ml and a 10 mg/ml FMN concentration. These samples were termed, FMN,*lc* (low coverage) and FMN,*hc* (high coverage) in the main text. The (n,m) chirality indices were assigned following previous reports³ and these assignment are listed in Table 1 of the main text.

Molecular Simulations:

A. Density Functional Theory Calculations:

Density Functional Theory (DFT) was used to determine the relative energy of the *syn*- and *anti*- conformers of *R*-FMN (FMN) and the corresponding electrostatic potential surface. Calculations were carried out with Gaussian 09⁴, at the B3LYP/6-31g+(d,p) DFT level⁵. The N(5)-N(10)-C(1') angle ω (shown in the Figure to the right) was constrained at three different values (110°, 115°, and 120°) representing typical sp^3 -conformations. Energy minimizations at these three angles resulted in a consistent 3 kcal/mol energy difference in favor of the *anti*-conformer. This energy difference reduces to 1.5 kcal/mol when water is added in conductor-like implicit solvent model. Thus, the results in vacuum (3 kcal/mol) and those in implicit water (1.5 kcal/mol) represent the two extreme dielectric constant environments, with the environment of the FMN helix wrapping SWNTs expected to be somewhere in between.



B. Molecular Mechanics Simulations of R-FMN helix onto either left-handed M-(6,8) or right-handed P-(8,6)-SWNTs. Cerius2 simulation software was utilized for molecular modeling using the Dreiding 2.21 force field for molecular mechanics, molecular dynamics and quenched dynamics simulations. The charge equilibration method was used to set atom charges for FMN, while zero charge was assigned for all SWNT carbon atoms, according to the literature.² Materials Studio 4 software was used for visualization. An sp^3 -hybridized geometry was used for the N atom at the 10 position (N(10)) of the

isoalloxazine ring (Figure 1e), while for the rest of the aromatic atoms, an sp^2 -configuration was utilized. The isoalloxazine ring of the energetically-favored Figure 1e conformation was utilized to construct δ_I helices around left-handed M -(6,8) or right-handed P -(8,6) nanotubes, in accordance to a previous report.² The isoalloxazine helices were minimized in a periodic boundary condition until RMS values are below 0.001 kcal/mol/atom, while the carbon nanotube was kept constrained on its energy minimized position. That position was obtained by minimizing the nanotube, within the same periodic boundary conditions, in the absence of FMN.

Table S1. UV-Vis-NIR maxima for FMN-wrapped and SDBS-replaced SWNTs as they relate to the E_{22}^S transitions of various left-handed SWNT chiralities.

Samples	Peak positions (nm)				
Left-handed SWNT indices	(5,6)	(4,8), (1,11)	(3,8), (5,9), (3,10), (5,7), (6,7)	(2,10), (7,8), (4,9), (6,8)	(1,12), (3,11), (5,10), (7,9)
FMN-wrapped SWNTs	565	607	664	743	816
SDBS-replaced SWNTs	559	593	649	730	808

Table S2. $\Sigma_n-\Sigma_{n+1}$ and $\Delta_n-\Delta_{n+1}$ sub-helix close contacts for the *M*-(6,8)-SWNT and *P*-(8,6)-SWNT within *P*-FMN helices.

<i>M</i>-(6,8)-SWNT within <i>P</i>-FMN Helix				
Distance (Å)				
Pair	C ₉ -H to bottom H of CH ₃ - at C ₇	C ₉ -H to top H of CH ₃ - at C ₇	N ₁ to H-C ₆	C=O to O=C
$\Sigma_1-\Sigma_2$	2.44	2.74		2.83
$\Sigma_2-\Sigma_3$	2.32	3.06		2.93
$\Sigma_3-\Sigma_4$	2.42	2.70		2.93
$\Sigma_4-\Sigma_5$	2.41	2.71		2.92
$\Sigma_5-\Sigma_6$	2.41	2.72		2.91
$\Sigma_6-\Sigma_7$	2.44	2.72		2.93
$\Sigma_7-\Sigma_8$	2.44	2.69		2.83
$\Sigma_8-\Sigma_1$	2.42	2.70		2.87
Average	2.41	2.76		2.89
Methyl (bottom and top) average		2.58		
Pair	C ₉ -H to bottom H of CH ₃ - at C ₇	C ₉ -H to top H of CH ₃ - at C ₇	N ₁ to H-C ₆	C=O to O=C
$\Delta_1-\Delta_2$	2.61	3.03	2.79	2.84
$\Delta_2-\Delta_3$	2.53	2.55	2.72	2.82
$\Delta_3-\Delta_4$	2.6	2.56	2.61	2.78
$\Delta_4-\Delta_5$	2.56	2.62	2.61	2.79
$\Delta_5-\Delta_6$	2.56	2.62	2.6	2.79
$\Delta_6-\Delta_7$	2.57	2.6	2.59	2.79
$\Delta_7-\Delta_8$	2.59	2.56	2.58	2.79
$\Delta_8-\Delta_1$	2.5	2.61	2.56	2.81
Average	2.57	2.64	2.63	2.80
Methyl (bottom and top) average		2.60		
Methyl ($\Sigma_M+\Delta_M$) average		2.59	Carbonyl average	2.85

<i>P</i>-(8,6)-SWNT within <i>P</i>-FMN Helix				
Pair	C ₉ -H to bottom H of CH ₃ - at C ₇	C ₉ -H to top H of CH ₃ - at C ₇	N ₁ to H-C ₆	C=O to O=C
$\Sigma_1-\Sigma_2$	2.55	2.6	2.6	2.8
$\Sigma_2-\Sigma_3$	2.55	2.6	2.6	2.79
$\Sigma_3-\Sigma_4$	2.57	2.67	2.61	2.79
$\Sigma_4-\Sigma_5$	2.58	2.61	2.6	2.79
$\Sigma_5-\Sigma_6$	2.58	2.57	2.6	2.79
$\Sigma_6-\Sigma_7$	2.52	2.61	2.74	2.81
$\Sigma_7-\Sigma_8$	2.44	2.6	2.65	2.78
$\Sigma_8-\Sigma_1$	2.4	2.74	2.73	2.76
Average	2.52	2.63	2.64	2.79
Methyl (bottom and top) average		2.57		
Pair	C ₉ -H to bottom H of CH ₃ - at C ₇	C ₉ -H to top H of CH ₃ - at C ₇	N ₁ to H-C ₆	C=O to O=C
$\Delta_1-\Delta_2$	2.42	2.72		2.94
$\Delta_2-\Delta_3$	2.43	2.71		2.94
$\Delta_3-\Delta_4$	2.42	2.73		2.92
$\Delta_4-\Delta_5$	2.42	2.7		2.91
$\Delta_5-\Delta_6$	2.42	2.74		2.92
$\Delta_6-\Delta_7$	2.4	2.72		2.91
$\Delta_7-\Delta_8$	2.48	2.72		2.86
$\Delta_8-\Delta_1$	2.42	2.7		2.83
Average	2.43	2.72		2.90
Methyl (bottom and top) average		2.57		
Methyl ($\Sigma_M+\Delta_M$) average		2.57	Carbonyl average	2.85

Table S3. Energy contributions (in kcal/mol) for the energy-minimized configurations of Figures S3(b&d) and S4(b&d).

Species	Bonds*	Angles*	Torsions*	Inversions*	vdW* with NT	vdW w/o NT	vdW <i>Difference</i>	E-S*	H-bonds*	Total
<i>M</i> -(6,8)-SWNT within <i>P</i> -FMN helix	97.1	82.6	21.6	0.6	203.2	572.3	-369.1	-491.4	-38.8	-125.0
<i>P</i> -(8,6)-SWNT within <i>P</i> -FMN helix	96.4	82.8	21.8	0.6	204.2	572.7	-368.5	-490.9	-38.7	-123.8
<i>Difference</i>	0.7	-0.2	-0.2	0.0	-1.0	-0.4	-0.6	-0.5	-0.1	-1.2

vdW: van der Waals interactions.

E-S: electrostatic interactions.

Energy terms indicated in asterisks compose the E_{total} .

Table S4. $\Sigma_n-\Sigma_{n+1}$ and $\Delta_n-\Delta_{n+1}$ sub-helix pair energy terms for the left-handed M -(6,8) and right-handed P -(8,6) within P -FMN helices.

M-(6,8)-SWNT within P-FMN Helix									
Pair	Bonds	Angles	Torsions	Inversions	VDW_w_NT	VDW_w/o_NT	Electrostatic	Total_w_NT	Total_w/o_NT
$\Sigma_1-\Sigma_2$	12.43	10.17	3.07	0.04	25.07	71.58	-45.93	4.84	51.36
$\Sigma_2-\Sigma_3$	12.13	10.19	3.07	0.04	25.06	72.04	-46.16	4.33	51.31
$\Sigma_3-\Sigma_4$	12.80	10.35	1.98	0.04	23.11	71.12	-46.39	1.90	49.90
$\Sigma_4-\Sigma_5$	12.99	10.30	1.99	0.04	22.28	70.92	-46.33	1.26	49.90
$\Sigma_5-\Sigma_6$	13.00	10.36	2.02	0.03	23.00	70.93	-46.25	2.17	50.09
$\Sigma_6-\Sigma_7$	13.13	10.60	2.09	0.03	24.28	70.85	-46.33	3.81	50.38
$\Sigma_7-\Sigma_8$	13.23	10.49	2.08	0.03	24.65	70.93	-45.93	4.55	50.83
$\Sigma_8-\Sigma_1$	13.21	10.29	2.00	0.03	24.23	70.75	-46.15	3.61	50.12
sum	102.93	82.77	18.30	0.28	191.68	569.11	-369.49	26.47	403.90
w - w/o						-377.43			-377.43
Pair	Bonds	Angles	Torsions	Inversions	VDW_w_NT	VDW_w/o_NT	Electrostatic	Total_w_NT	Total_w/o_NT
$\Delta_1-\Delta_2$	11.74	10.27	3.13	0.09	26.01	71.46	-47.12	4.11	49.56
$\Delta_2-\Delta_3$	11.18	9.84	3.44	0.11	27.77	71.94	-46.84	5.49	49.66
$\Delta_3-\Delta_4$	11.12	10.04	3.14	0.12	27.99	72.18	-46.53	5.89	50.07
$\Delta_4-\Delta_5$	11.15	10.40	3.07	0.12	27.32	72.16	-46.82	5.23	50.07
$\Delta_5-\Delta_6$	11.26	10.46	3.11	0.11	27.27	72.09	-46.87	5.34	50.16
$\Delta_6-\Delta_7$	11.28	10.40	3.18	0.11	27.19	71.98	-46.80	5.36	50.15
$\Delta_7-\Delta_8$	11.51	10.49	3.09	0.11	27.00	71.76	-46.90	5.30	50.06
$\Delta_8-\Delta_1$	12.01	10.62	2.80	0.10	26.60	71.99	-47.26	4.87	50.26
sum	91.24	82.52	24.97	0.87	217.14	575.55	-375.15	41.59	400.00
w - w/o	97.08	82.64	21.63	0.58	204.41	-358.41	-372.32	34.03	-358.41

P-(8,6)-SWNT within P-FMN Helix									
Pair	Bonds	Angles	Torsions	Inversions	VDW_w_NT	VDW_w/o_NT	Electrostatic	Total_w_NT	Total_w/o_NT
$\Sigma_1-\Sigma_2$	11.36	10.49	3.26	0.12	26.55	71.93	-47.01	4.76	50.14
$\Sigma_2-\Sigma_3$	11.21	10.48	3.18	0.12	27.58	72.09	-46.93	5.64	50.15
$\Sigma_3-\Sigma_4$	11.27	10.42	3.11	0.12	27.03	71.98	-46.86	5.09	50.03
$\Sigma_4-\Sigma_5$	11.21	10.30	3.04	0.11	27.55	72.12	-46.75	5.46	50.03
$\Sigma_5-\Sigma_6$	11.23	10.13	3.17	0.11	27.94	72.13	-46.74	5.84	50.03
$\Sigma_6-\Sigma_7$	11.35	10.23	3.34	0.11	26.92	71.76	-46.87	5.08	49.93
$\Sigma_7-\Sigma_8$	10.88	10.03	4.11	0.09	27.10	72.48	-46.98	5.23	50.60
$\Sigma_8-\Sigma_1$	10.97	10.05	4.08	0.10	26.43	72.39	-46.83	4.80	50.76
sum	89.49	82.12	27.28	0.88	217.09	576.87	-374.97	41.89	401.68
w - w/o						-359.79			-359.79
Pair	Bonds	Angles	Torsions	Inversions	VDW_w_NT	VDW_w/o_NT	Electrostatic	Total_w_NT	Total_w/o_NT
$\Delta_1-\Delta_2$	12.99	10.38	2.20	0.04	23.46	70.85	-46.48	2.58	49.97
$\Delta_2-\Delta_3$	13.05	10.27	2.07	0.03	24.24	70.78	-46.39	3.26	49.80
$\Delta_3-\Delta_4$	12.97	10.31	1.99	0.04	24.63	70.90	-46.31	3.62	49.89
$\Delta_4-\Delta_5$	13.03	10.32	1.96	0.04	23.83	70.95	-46.28	2.88	50.00
$\Delta_5-\Delta_6$	12.90	10.32	1.92	0.03	24.18	71.12	-46.34	3.01	49.95
$\Delta_6-\Delta_7$	12.69	10.52	2.06	0.03	25.41	71.40	-46.37	4.35	50.34
$\Delta_7-\Delta_8$	12.81	10.70	2.02	0.03	24.28	71.29	-46.37	3.48	50.49
$\Delta_8-\Delta_1$	12.91	10.61	2.04	0.04	23.22	71.17	-46.33	2.48	50.43
sum	103.34	83.42	16.28	0.28	193.24	568.46	-370.89	25.67	400.88
w - w/o	96.41	82.77	21.78	0.58	205.17	-375.22	-372.93	33.78	-375.21

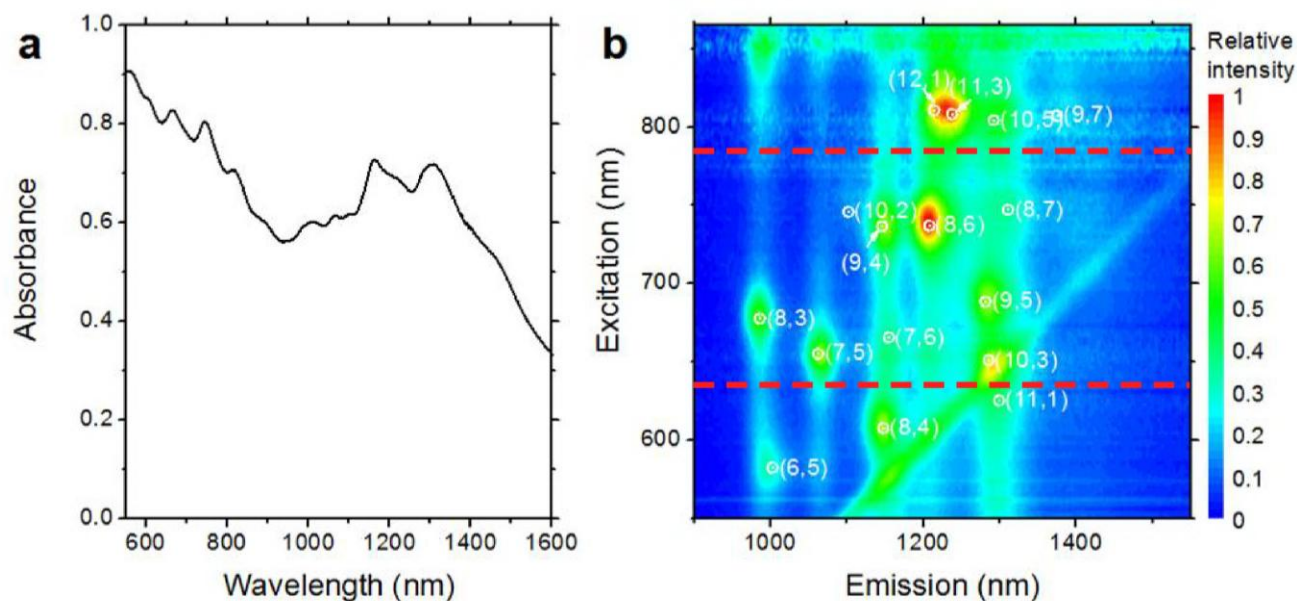


Figure S1. (a) UV-Vis-NIR spectrum and (b) PLE map of FMN-wrapped HiPco SWNTs, along with peak assignments[†] according to the literature (Ju, S.-Y. *et al.*, *Nature Nanotech.* 3, 356-362 (2008)).

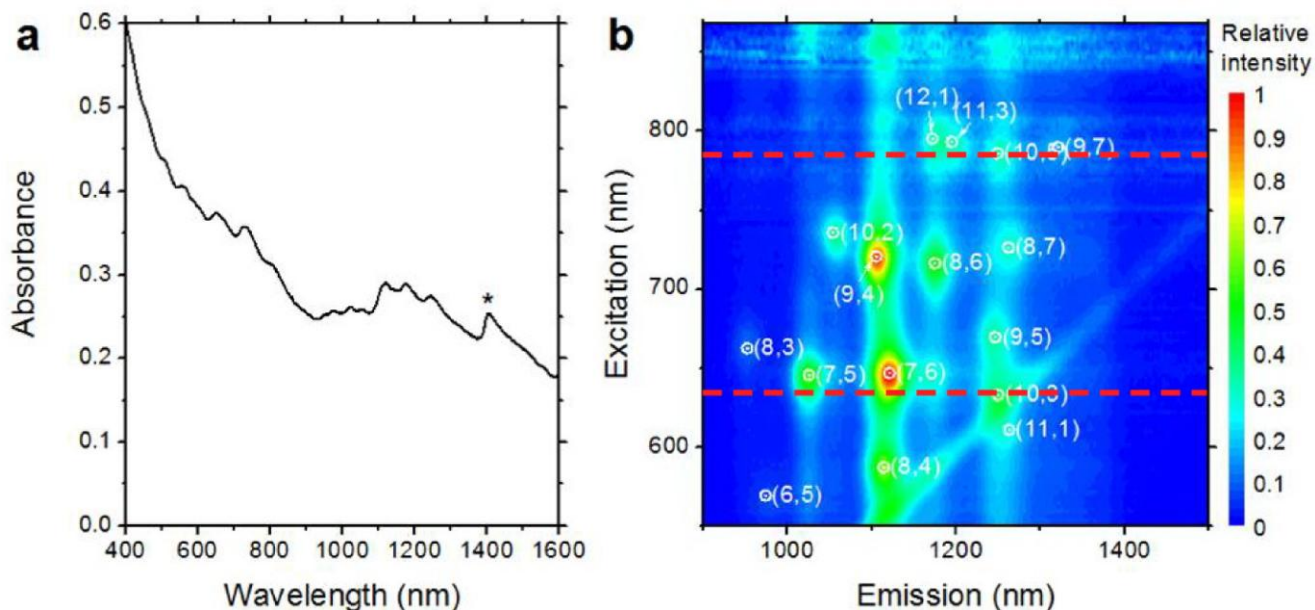


Figure S2. (a) UV-Vis-NIR spectrum and (b) PLE map of FMN-extracted and SDBS-replaced HiPco SWNTs, along with peak assignments[†] according to the literature (Bachilo, S. M. *et al.*, *Science*, 298, 2361-2366 (2002)). Star in figure (a) indicates water contamination due to repetitive dialysis steps required to extract out FMN. Dashed red lines indicate excitation wavelengths for the two laser lines (785 and 633 nm) used in Figure S7.

[†] For the sake of clarity, the traditional nomenclature were used to assign the (n,m) values of SWNTs, as opposed to the left-handed enriched (m,n) notation.

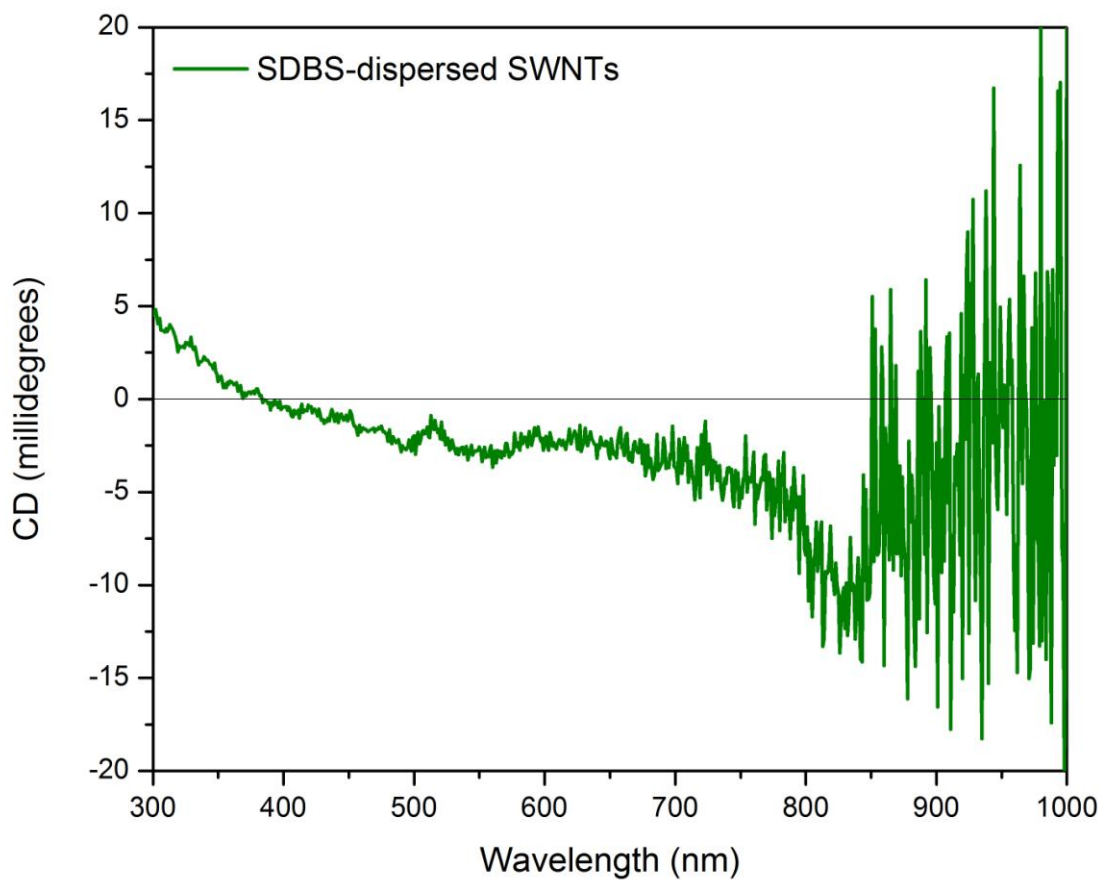


Figure S3. Circular dichroism (CD) of SDBS-dispersed HiPco SWNTs.

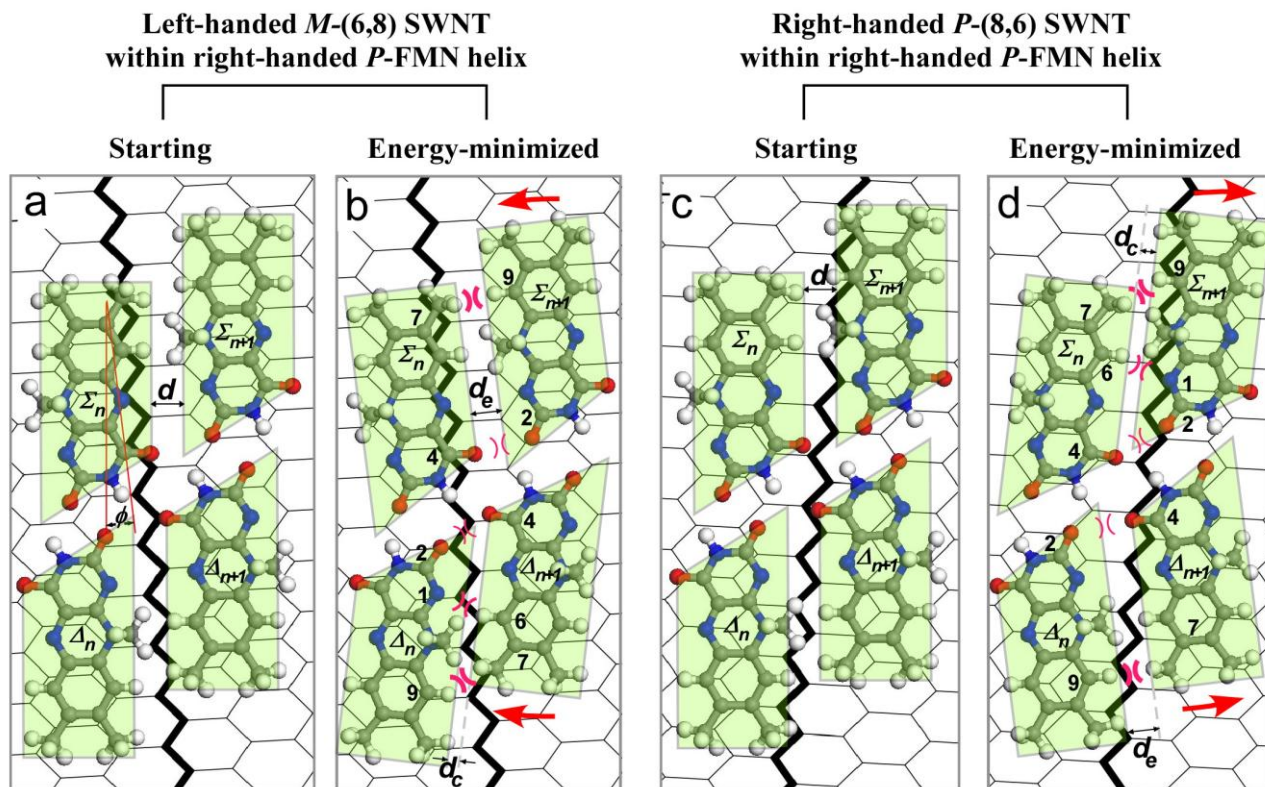


Figure S4. Atomistic molecular simulation of starting (a & c) and energy-minimized (b & d) of the left-handed M -(6,8) SWNT and right-handed P -(8,6) SWNT within right-handed P -FMN helices, respectively. The P -FMN helix is composed of two sub-helices (Σ_n and Δ_n). Upon energy minimization, the isoalloxazine rings of Σ_n and Δ_n sub-helices rotate opposite to each other so that only one sub-helix (*i.e.* Σ_n) improves its alignment with the nanotube lattice.

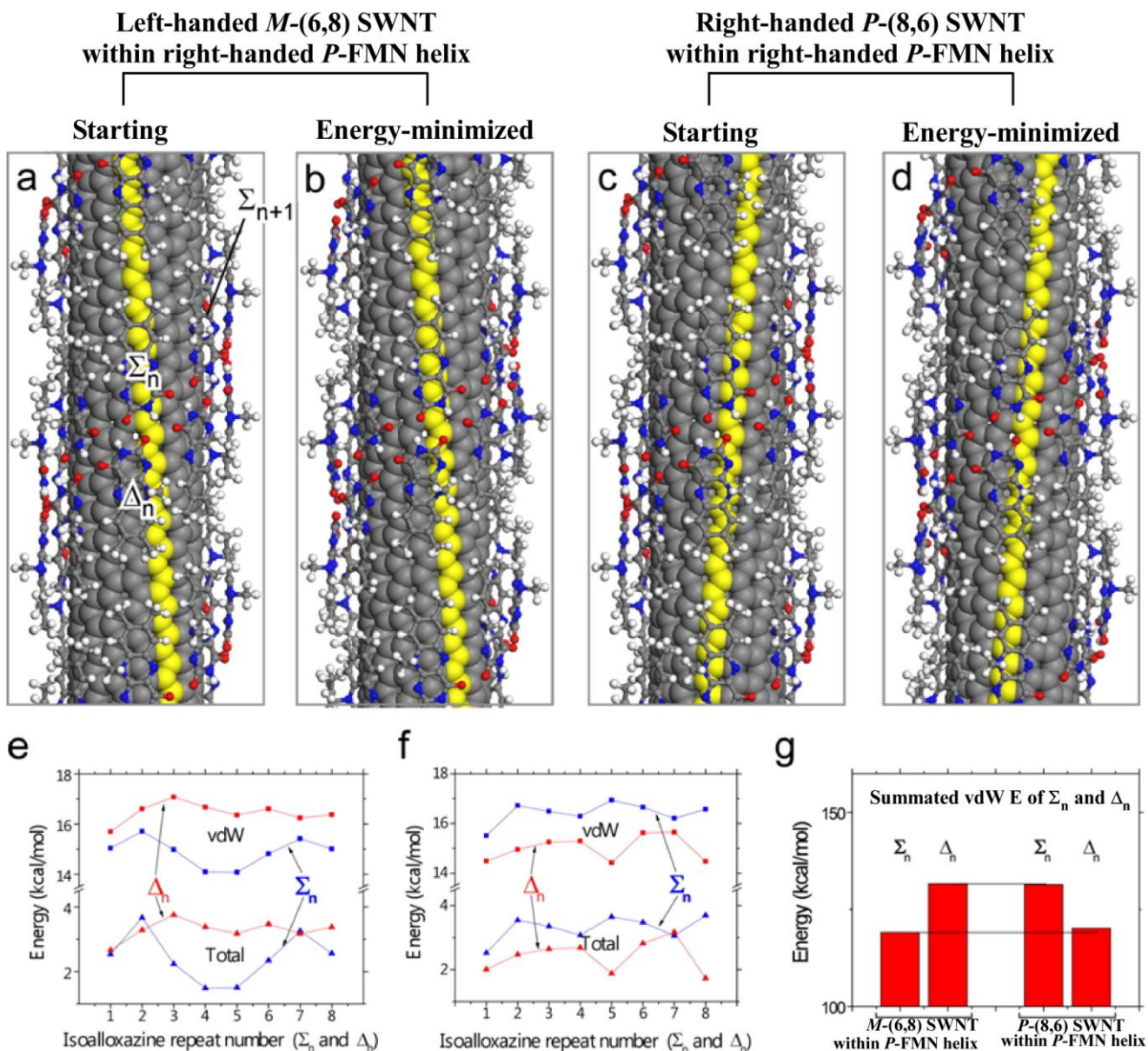


Figure S5. (a-d) 3-D rendering of Figure S3. (e & f) vdW and total energy contributions for all 8 Σ_n and Δ_n isoalloxazine units for (b&d), respectively. (g) Summated vdW energy for both Σ_n and Δ_n isoalloxazine sub-helices for the left-handed $M-(6,8)$ -SWNT and right-handed $P-(8,6)$ -SWNT within the right-handed P -FMN helix complexes of (b&d), respectively.

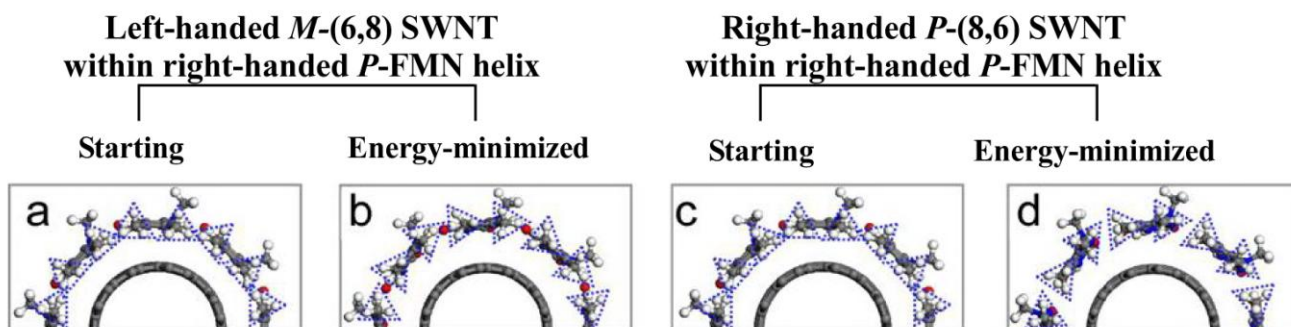


Figure S6. Starting (a & c) and energy minimized (b & d) conformations of the dimethyl moieties of the isoalloxazine rings. The dotted blue triangles are to guide the eye and indicate interdigitation.

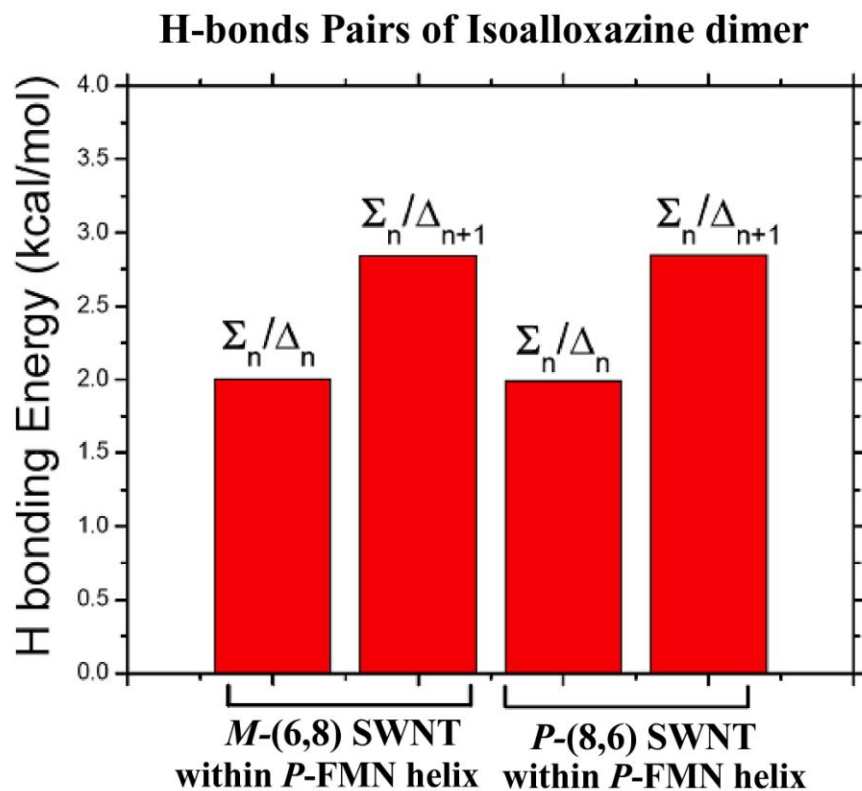


Figure S7. Average H-bonding energy between Σ_n and Δ_n as well as Σ_n and Δ_{n+1} isoalloxazine pairs for the energy-minimized left-handed *M*-(6,8) SWNT and right-handed *P*-(8,6) SWNT within right-handed *P*-FMN helix .

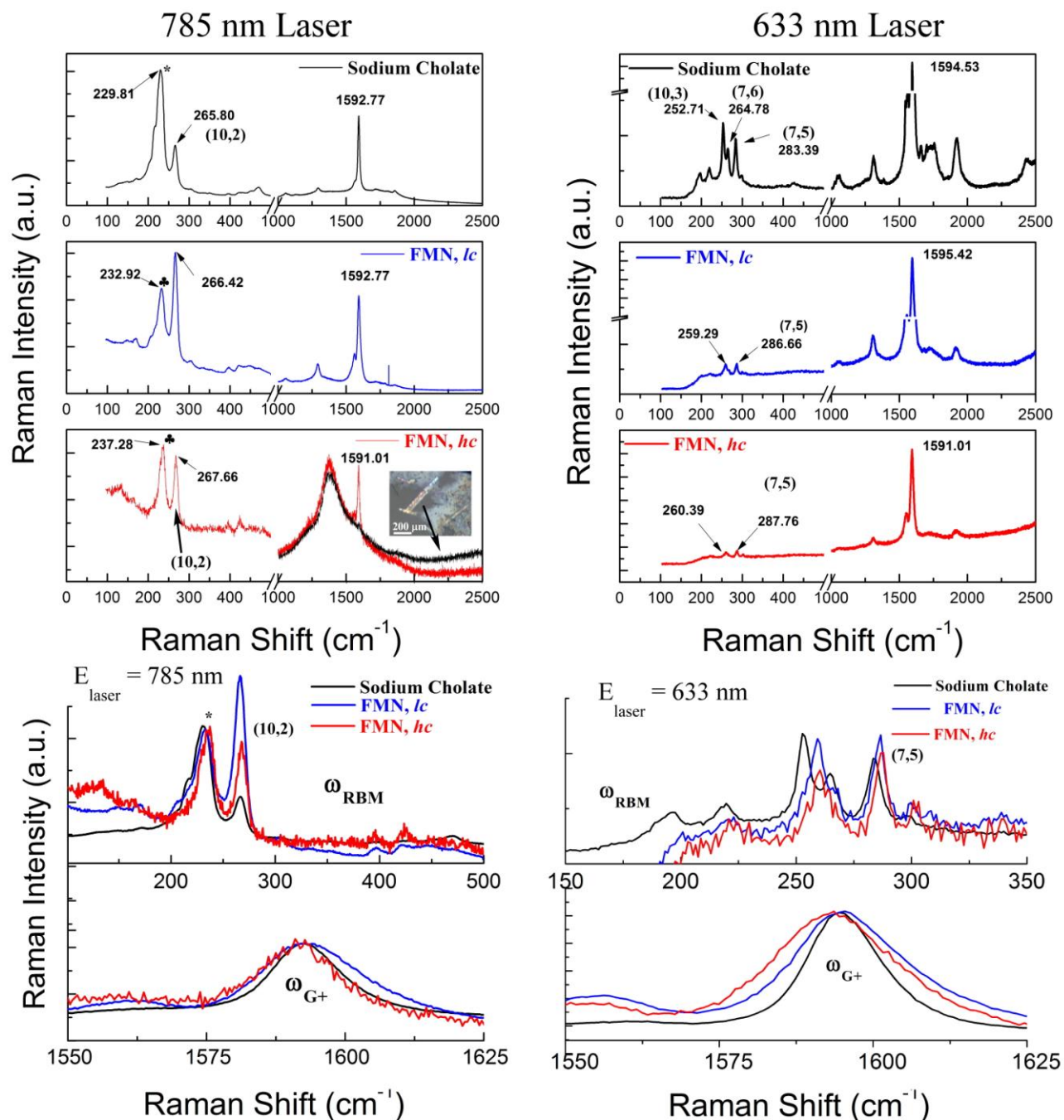


Figure S8. Resonance Raman Spectra of SC- and FMN-dispersed SWNTs (with low (*lc*) and high (*hc*) FMN coverage) at 785 nm (left) and 633nm (right) excitation (E_{laser}) wavelengths in survey/stacked (top) and zoom-in/overlaid (bottom) format for the RBM and G modes. The black curve in the FMN, *hc* sample (right) corresponds to the RRS from an FMN crystal, whose micrograph is shown at the corresponding inset. As discussed in the assignment graph of Figure S9, in the case of SC, the RBM peak denoted with the symbol (*) is initially composed of (10,5), (11,3), (12,1) SWNTs. In the case of FMN, the same RBM peak that is now denoted with the symbol (\clubsuit), gains additional contributions from (8,7) and (8,6) SWNTs, along with the original (10,5), (11,3), (12,1) nanotubes (Figure S9). Similarly, for the 633 nm laser, the respective assignment of (10,3) and (7,6) for the 252.7 and 264.8 cm^{-1} maxima for SC do not hold for FMN, since their redshifted E_{22}^S transitions brings in resonance the (11,1)-SWNT specie (Figure S9).

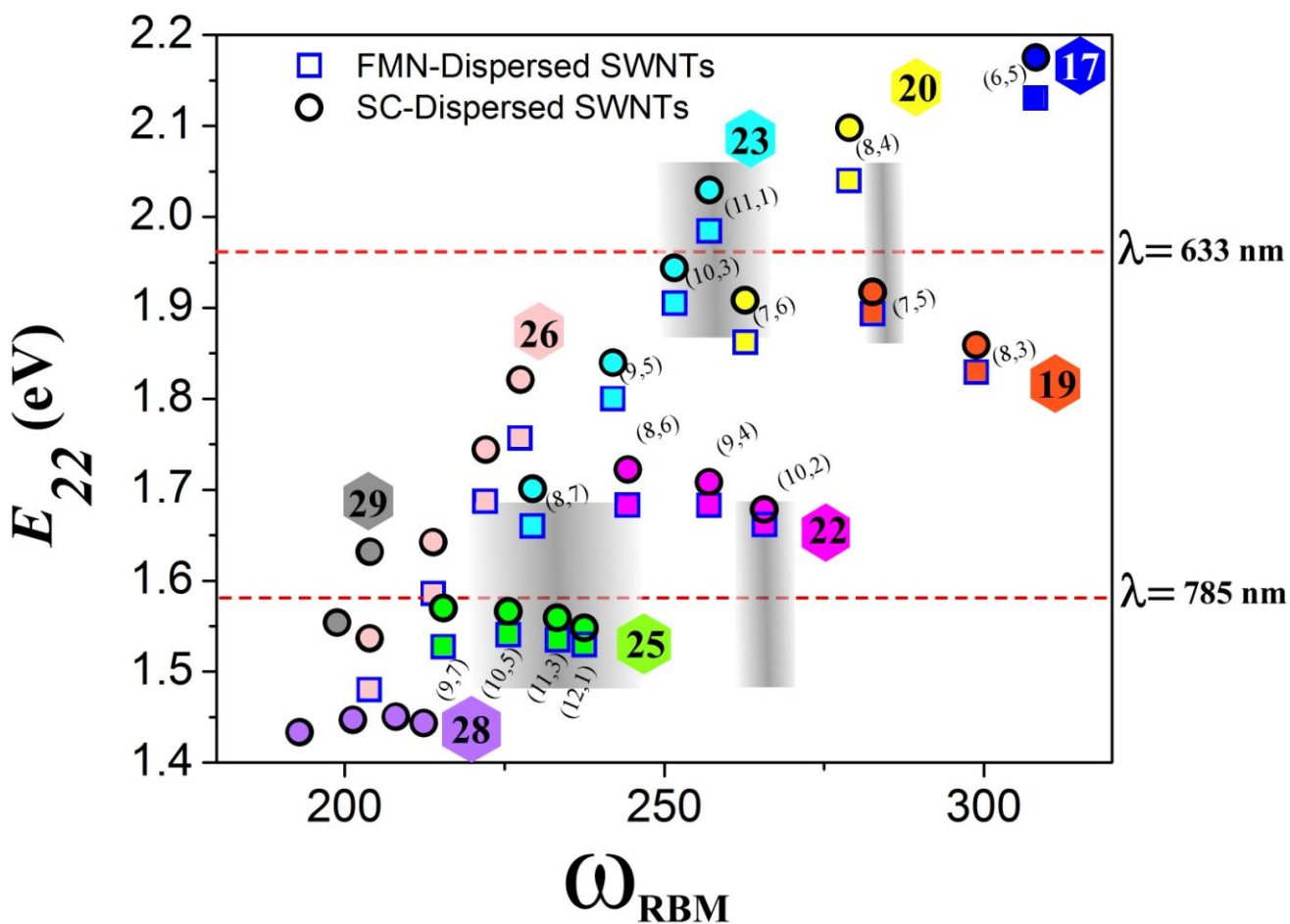


Figure S9. PLE-derived $sem-E_{22}$ transitions plotted against RBM-calculated resonances for the observed sem -SWNTs based on the $\omega_{RBM} = \alpha/d_t + \beta$, with $\alpha=223.5 \text{ cm}^{-1}/\text{nm}$ and $\beta = 12.5 \text{ cm}^{-1}$ formula for individualized SWNTs.^{6,7,8} The two excitation lasers used in Figure S8 are shown as dashed red lines. Each $2n+m$ nanotube family is color-coded and the nanotubes of interest are identified with their (n,m) values. The profound redshift in E_{22}^S transitions from SC to FMN is shown for all (n,m) -SWNTs that FMN suspends and denoted with circles and squares, respectively. The four vertical grey bands illustrate resonance conditions associated with the full width at half maximum (FWHM) of the assigned peaks observed in Figure S8. Due to nanotube crowding, the lower frequency peaks are composites of multiple (n,m) -SWNTs in resonance, as opposed to the higher frequency peaks tabulated in Table 1 of main text. The Raman shift and relative intensity of the assigned RBM features in Figure S8 are discussed below:

785 nm Laser

230 cm^{-1} peak for SC: This RBM feature is denoted with the (*) symbol since it possesses contributions from the (10,5), (11,3) and (12,1)-SWNTs that are in resonance for the SC environment (green circles).

233 and 237 cm^{-1} peaks for FMN, (*lc* and *hc*, respectively): These RBM features, denoted with the (♣) symbol, possess contributions not only from the (10,5), (11,3) and (12,1)-SWNTs, but also from the (8,7) and (8,6)-SWNTs. This originates from the significantly higher charge transfer of FMN that results in an appreciable redshift for all (n,m) -SWNTs. Such redshift moves the original (10,5), (11,3) and (12,1)-SWNTs away from resonance, while gradually increasing the resonance conditions for the (8,7) and (8,6)-SWNTs. This, together with the reported tendency of FMN to enrich (8,6)-SWNTs,

explains the substantial upshift in RBM frequency from *lc* to *hc* samples.

265.8 cm⁻¹ peak for SC: The lower nanotube crowding in the higher frequency RBM region spaces the (10,2) nanotube considerably farther from the neighboring (9,4) specie. The (9,4) is expected to peak at 257 cm⁻¹. Consequently, the appreciable sharpness of the 266.8 cm⁻¹ peak (full-width-at-half-maximum (FWHM) spanning from 259 to 273 cm⁻¹) renders this RBM feature solely attributed to the (10,2)-SWNT.

266.4 and 267.7 cm⁻¹ peaks for FMN, (*lc* and *hc*, respectively): The retained sharpness of these features signify that (10,2)-SWNT remains the prime contributor for these peaks, and the observed redshift must originate from nanotube twisting.

SC-observed relative intensity between the 230 and 265.8 cm⁻¹ peaks: The appreciable proximity of the 785 nm laser line to the (10,5), (11,3) and (12,1)-SWNTs as opposed to the (10,2) species renders the 230 cm⁻¹ peak significantly more intense than the 265.8 cm⁻¹ peak for the SC-dispersed nanotube sample.

FMN-observed relative intensity between the 233-237 and 266-267 cm⁻¹ peaks: The higher charge transfer of FMN moves the (10,5), (11,3) and (12,1)-SWNTs away from resonance. This causes a profound intensity decrease for these features and while the (8,7) and (8,6)-SWNTs gradually move closer to resonance, they can not compensate for the intensity loss. On the other hand, the charge transfer experienced by the (10,2) brings its E_{22}^S transition closer to the 785 line and substantially increases its intensity. This explains the intensity reversal for these two peaks from the SC to FMN, *lc* sample. In the case of FMN, *hc* sample, further increase in charge transfer moves the (8,6) specie closer to resonance, which balances the intensity ratio between the two peaks.

633 nm Laser

Composite feature peaking at 252.7 and 264.8 cm⁻¹ (SC): For SC-dispersed SWNTs, the (10,3) and (7,6) assignments for the respective 252.7 and 264.8 cm⁻¹ maxima are based on the fact that these nanotubes are closer in resonance than the (11,1) SWNT.

Composite feature peaking at 259.3 and 260.4 cm⁻¹ for FMN (*lc* and *hc* respectively): In the case of FMN, the significant redshift in their E_{22}^S transitions moves the (10,3) and (7,6) away from resonance and the (11,1) closer to resonance, which explains why we go from two peaks in the SC sample to one peak in the FMN samples.

Individual peaks at 283.4 cm⁻¹ (SC), 286.7 cm⁻¹ (FMN, *lc*) and 287.8 cm⁻¹ (FMN, *hc*): The lower nanotube crowding in the higher frequency RBM region spaces the (7,5) nanotube considerably farther from the neighboring (8,4) and (8,3) species. The relatively sharp peak at 283.4 cm⁻¹ with FWHM spanning from 280.4 to 286.4 cm⁻¹ is positioned far enough from the (8,4) and (8,3) (expected to peak at 279 and 299 cm⁻¹, respectively) to be safely assigned as the RBM frequency primarily from the (7,5) specie. Moreover these nanotubes are both disfavored in terms of resonance. Consequently, the observed redshift must originate from nanotube twisting of the (7,5)-SWNT.

Small peak at 298 cm⁻¹ (SC), 299 cm⁻¹ (FMN, *lc*) and 302 cm⁻¹ (FMN, *hc*): This faint peak is clearly attributed to (8,3)-SWNT on the right of the sharp peak, with maximum between 283 and 289 cm⁻¹. Similarly to (7,5), the (8,3) also displays the characteristic redshift pattern that is discussed in the main text as evidence of FMN-induced nanotube torsion.

REFERENCES

1. Nikolaev, P.; Bronikowski, M. J.; Bradley, R. K.; Rohmund, F.; Colbert, D. T.; Smith, K. A.; Smalley, R. E., *Chem. Phys. Lett.* **1999**, 313, 91-97.
2. Ju, S. Y.; Doll, J.; Sharma, I.; Papadimitrakopoulos, F., *Nat. Nanotechnol.* **2008**, 3 (6), 356-362.
- 3 (a) Jorio, A.; Fantini, C.; Pimenta, M. A.; Capaz, R. B.; Samsonidze, G. G.; Dresselhaus, G.; Dresselhaus, M. S.; Jiang, J.; Kobayashi, N.; Grüneis, A.; Saito, R., *Phys. Rev. B* **2005**, 71 (7); (b) Fantini, C.; Jorio, A.; Souza, M.; Strano, M. S.; Dresselhaus, M. S.; Pimenta, M. A., *Phys. Rev. Lett.* **2004**, 93 (14), 147406-1-147406-4.
4. Frisch, M. J. T., G. W.; Schlegel, H. B.; Scuseria, G. E.; Robb, M. A.; Cheeseman, J. R.; Scalmani, G.; Barone, V.; Mennucci, B.; Petersson, G. A.; Nakatsuji, H.; Caricato, M.; Li, X.; Hratchian, H. P.; Izmaylov, A. F.; Bloino, J.; Zheng, G.; Sonnenberg, J. L.; Hada, M.; Ehara, M.; Toyota, K.; Fukuda, R.; Hasegawa, J.; Ishida, M.; Nakajima, T.; Honda, Y.; Kitao, O.; Nakai, H.; Vreven, T.; Montgomery, Jr., J. A.; Peralta, J. E.; Ogliaro, F.; Bearpark, M.; Heyd, J. J.; Brothers, E.; Kudin, K. N.; Staroverov, V. N.; Kobayashi, R.; Normand, J.; Raghavachari, K.; Rendell, A.; Burant, J. C.; Iyengar, S. S.; Tomasi, J.; Cossi, M.; Rega, N.; Millam, N. J.; Klene, M.; Knox, J. E.; Cross, J. B.; Bakken, V.; Adamo, C.; Jaramillo, J.; Gomperts, R.; Stratmann, R. E.; Yazyev, O.; Austin, A. J.; Cammi, R.; Pomelli, C.; Ochterski, J. W.; Martin, R. L.; Morokuma, K.; Zakrzewski, V. G.; Voth, G. A.; Salvador, P.; Dannenberg, J. J.; Dapprich, S.; Daniels, A. D.; Farkas, Ö.; Foresman, J. B.; Ortiz, J. V.; Cioslowski, J.; Fox, D. J. *Gaussian 09, Revision A.1.*, Wallingford CT, **2009**.
5. Chai, J.-D.; Head-Gordon, M., *Phys. Chem. Chem. Phys.* **2008**, 10 (44), 6615-6620.
6. Bachilo, S. M.; Strano, M. S.; Kittrell, C.; Hauge, R. H.; Smalley, R. E.; Weisman, R. B., *Science* **2002**, 298 (5602), 2361.
7. Luo, Z.; Li, R.; Sang, N. K.; Papadimitrakopoulos, F., *Phys. Rev. B* **2004**, 70 (24), 1-8.
8. Abanulo, D. C.; Badalucco, C. A.; Gascón, J. A.; Dobrynin, A. V.; Yang, Y.; Hagan, M. F.; Hu, B.; Ju, S.-Y.; Doll, J. D.; Papadimitrakopoulos, F., *Submitted* **2012**.

References

1. Nikolaev, P.; Bronikowski, M. J.; Bradley, R. K.; Rohmund, F.; Colbert, D. T.; Smith, K. A.; Smalley, R. E., *Chem. Phys. Lett.* **1999**, 313, 91-97.
2. Ju, S. Y.; Doll, J.; Sharma, I.; Papadimitrakopoulos, F., *Nat. Nanotechnol.* **2008**, 3 (6), 356-362.
3. (a) Jorio, A.; Fantini, C.; Pimenta, M. A.; Capaz, R. B.; Samsonidze, G. G.; Dresselhaus, G.; Dresselhaus, M. S.; Jiang, J.; Kobayashi, N.; Grüneis, A.; Saito, R., *Phys. Rev. B* **2005**, 71 (7); (b) Fantini, C.; Jorio, A.; Souza, M.; Strano, M. S.; Dresselhaus, M. S.; Pimenta, M. A., *Phys. Rev. Lett.* **2004**, 93 (14), 147406-1-147406-4.
4. Frisch, M. J. T., G. W.; Schlegel, H. B.; Scuseria, G. E.; Robb, M. A.; Cheeseman, J. R.; Scalmani, G.; Barone, V.; Mennucci, B.; Petersson, G. A.; Nakatsuji, H.; Caricato, M.; Li, X.; Hratchian, H. P.; Izmaylov, A. F.; Bloino, J.; Zheng, G.; Sonnenberg, J. L.; Hada, M.; Ehara, M.; Toyota, K.; Fukuda, R.; Hasegawa, J.; Ishida, M.; Nakajima, T.; Honda, Y.; Kitao, O.; Nakai, H.; Vreven, T.; Montgomery, Jr., J. A.; Peralta, J. E.; Ogliaro, F.; Bearpark, M.; Heyd, J. J.; Brothers, E.; Kudin,

- K. N.; Staroverov, V. N.; Kobayashi, R.; Normand, J.; Raghavachari, K.; Rendell, A.; Burant, J. C.; Iyengar, S. S.; Tomasi, J.; Cossi, M.; Rega, N.; Millam, N. J.; Klene, M.; Knox, J. E.; Cross, J. B.; Bakken, V.; Adamo, C.; Jaramillo, J.; Gomperts, R.; Stratmann, R. E.; Yazyev, O.; Austin, A. J.; Cammi, R.; Pomelli, C.; Ochterski, J. W.; Martin, R. L.; Morokuma, K.; Zakrzewski, V. G.; Voth, G. A.; Salvador, P.; Dannenberg, J. J.; Dapprich, S.; Daniels, A. D.; Farkas, Ö.; Foresman, J. B.; Ortiz, J. V.; Cioslowski, J.; Fox, D. J., 2009.
5. Chai, J.-D.; Head-Gordon, M., *Phys. Chem. Chem. Phys.* **2008**, *10* (44), 6615-6620.
 6. Bachilo, S. M.; Strano, M. S.; Kittrell, C.; Hauge, R. H.; Smalley, R. E.; Weisman, R. B., *Science* **2002**, *298* (5602), 2361.
 7. Luo, Z.; Li, R.; Sang, N. K.; Papadimitrakopoulos, F., *Phys. Rev. B* **2004**, *70* (24), 1-8.
 8. Abanulo, D. C.; Badalucco, C. A.; Gascón, J. A.; Dobrynin, A. V.; Yang, Y.; Hagan, M. F.; Hu, B.; Ju, S.-Y.; Doll, J. D.; Papadimitrakopoulos, F., *Submitted* **2012**.